


Nonuniformities in miscible two-layer two-component thin liquid films

Christopher Larsson  and Satish Kumar**Department of Chemical Engineering and Materials Science, University of Minnesota,
Minneapolis, Minnesota 55455, USA* (Received 23 November 2020; accepted 26 February 2021; published 26 March 2021)

Depositing and obtaining a liquid film of uniform thickness is a problem integral to numerous applications and requires an understanding of capillary leveling, Marangoni flows, evaporation, and various other phenomena. These applications often demand multilayer films where each layer has distinct properties, and this gives rise to additional challenges. It has been experimentally demonstrated that two-layer films in which the layers are miscible can undergo dewetting, but theoretical understanding of this phenomenon is lacking. Through a lubrication-theory-based model, this work studies the mechanisms that may initiate dewetting in miscible two-layer two-component films. The model film consists of nonvolatile solvent and solute with constant density and viscosity. Two coupled fourth-order nonlinear partial differential equations describing the time evolution of the film height and solute concentration are derived and then solved with a pseudospectral method. It is found that a disparity in initial solute concentration between the film layers drives flows that lead to significant film-height nonuniformities. A parametric study is conducted to examine the influence of system parameters on this behavior and to develop several scaling relations that shed light on the underlying physical mechanisms.

DOI: [10.1103/PhysRevFluids.6.034004](https://doi.org/10.1103/PhysRevFluids.6.034004)

I. INTRODUCTION

Ranging from the production of organic light-emitting diode screens [1], printed electronics [2], and pharmaceuticals [3] to the tear film protecting our eyes [4,5], thin liquid films are ubiquitous; they exhibit many fascinating and exploitable behaviors that underlie numerous industrial processes. These processes produce lithium-ion batteries [6], solar and fuel cells [7], drug-delivery devices [3], and many other products where desired functionality requires that the films have controlled thickness and species concentration distributions.

Advanced applications often require that coated films consist of numerous layers with varying components. These films are deposited through a number of processes such as slot coating, curtain coating, and spray coating. However, small perturbations from vibrations, imperfect mixing, and other sources can cause variations in film height and component concentration with potentially disastrous effects on coating quality. While variations in the film height generate capillary flows that level the film, variations in component concentration can cause surface-tension gradients and thus Marangoni flow. Sufficiently strong Marangoni flow leads to film rupture (dewetting) and is catastrophic to coating quality. However, even minor instabilities that result in small nonuniformities may cause a significant quality degradation, so it is crucial to understand the evolution of nonuniformities in thin liquid films.

The growth of nonuniformities in liquid films from Marangoni flow has been extensively studied in one-layer systems [8,9]. The characteristic case of a binary (two-component) film has received considerable attention because it forms a foundation from which we may understand more complex

*kumar030@umn.edu

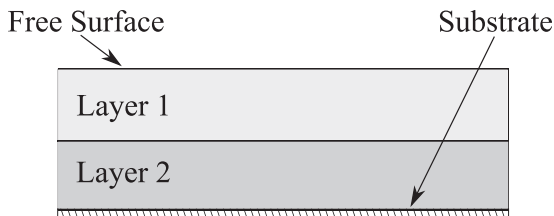


FIG. 1. Schematic of a two-layer liquid film resting on a solid substrate. If the liquid layers are miscible, there is no distinct interface between them.

systems. Serpetsi and Yiantsios [10] studied the stability of an evaporating one-layer binary film through linear stability analysis and nonlinear simulations, finding modes of instability similar to those investigated by Pearson [11] and Scriven and Sternling [12,13]. Including a variable viscosity, Yiantsios *et al.* [14] examined the nonlinear evolution of film-height and concentration nonuniformities in drying polymer films. Furthermore, the influence of substrate geometry [15,16], soluble and insoluble surfactants [4,15,17], evaporation rate [10,15,18,19], and colloidal particles [15,19,20] has been extensively explored in one-layer systems.

However, coated films are often comprised of multiple liquid layers to provide advanced functionality [21–24]. Horiuchi *et al.* [25] experimentally demonstrated dewetting of two-layer miscible films resting on solid substrates, but current theoretical understanding is largely limited to the case of immiscible liquids [26–31]. Figure 1 shows a simple schematic of a two-layer film resting on a substrate with a deformable liquid-air interface (free surface). While the liquid-liquid interface between layers is depicted sharply in Fig. 1, it may be diffuse or even nonexistent if the layers are miscible. Through two-layer slot coating, Horiuchi *et al.* [25] coated two-layer films with an alcohol-based bottom layer and water-based top layer and examined the influence of liquid properties and film thickness ratios on dewetting. Because these layers are miscible, the only distinct fluid-fluid interface is the free surface depicted in Fig. 1.

When modeling species concentration in multicomponent films, many previous studies have employed a rapid-vertical-diffusion approximation [15,17,32–34]. To leading order, this approximation assumes species concentration is uniform through the film depth. This hinges on the assumptions that initial vertical concentration gradients are negligible and that vertical diffusion is rapid in comparison to other process time scales. Consequently, this approximation is not useful for studying two-layer films where there may be a significant difference in species concentration between layers resulting in large vertical gradients. Although some previous work on the stability of liquid films has accounted for the presence of vertical concentration gradients [4,10,14,16], there is limited understanding of their role in miscible multilayer films where large vertical gradients may be present initially. Fundamental understanding of the stability of miscible multilayer films is important in numerous coating applications [25], but to the best of our knowledge a systematic theoretical investigation of the evolution of miscible multilayer films has yet to be reported.

In this work, we study the model problem of a nonvolatile two-layer binary film that approximates the conditions studied by Horiuchi *et al.* [25] (Fig. 1). The primary goal of this paper is to understand the mechanisms that generate film-height nonuniformities in two-layer miscible films rather than to attempt a quantitative comparison with the experiments of Horiuchi *et al.* [25]. To focus on the effects of solutal Marangoni flow, we choose to neglect evaporation and thermal Marangoni flows in this study. The rest of the paper is organized as follows. In Sec. II, we present the mathematical model. In Sec. III, we identify regions of the problem parameter space with qualitatively different dynamics. We also develop analytical expressions that provide insight into the underlying physical mechanisms. In Sec. IV, we present a parametric study to highlight the key factors influencing film uniformity. Conclusions are given in Sec. V.

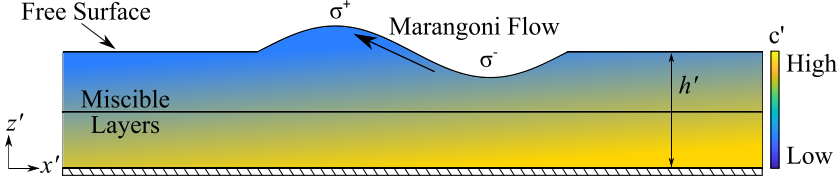


FIG. 2. Schematic of the model geometry of two miscible liquid layers resting on a solid substrate. One liquid is considered the “solvent” and the other the “solute.” Yellow indicates a higher concentration of solute, and σ^+ denotes a locally high surface tension and σ^- denotes a locally low surface tension that arise from solute concentration gradients. The resulting surface-tension gradient causes formation of a film-height nonuniformity, through Marangoni flow, from an initially flat interface (see Fig. 1).

II. MATHEMATICAL MODEL

We model the evolution of film height and species concentration in a thin liquid film resting on a solid substrate as shown in Fig. 2. Film height $h' = h'(t', x')$ and solute concentration $c' = c'(t', x', z')$ vary with time t' and the spatial variables x' and z' . The liquid is comprised of two miscible liquids, one of which is labeled the “solvent” and the other the “solute.” When the solvent and solute surface tensions differ, solute concentration gradients create Marangoni stresses that drive Marangoni flow at the liquid-air interface (free surface) as depicted in Fig. 2. We enforce periodic conditions in x' , assuming edge effects are negligible, and neglect evaporation and thermal Marangoni flows to focus on the effects of solutal Marangoni flow.

A. Hydrodynamics

The liquid film is assumed Newtonian with constant viscosity μ and density ρ . Surface tension σ' is scaled by the solvent surface tension σ_0 , and the solute concentration c' by an initial concentration c_0 . The vertical coordinate z' is scaled by the initial film height H , while the lateral coordinate x' is scaled by the length scale L obtained from balancing viscous and Marangoni stresses at the interface:

$$\mu \frac{\sigma_0 H^2}{\mu L^3} \sim \frac{\Delta \sigma \omega_0}{L} \Rightarrow L \sim \frac{H}{\sqrt{\text{Ma}}}. \quad (1)$$

The viscous scale used in this balance is based on a capillary velocity and arises from considering mass and x -momentum balances. The Marangoni number $\text{Ma} = \Delta \sigma \omega_0 / \sigma_0$, where $\Delta \sigma$ is the solvent and solute surface-tension difference (assumed positive), and ω_0 is the initial mass or mole fraction of solute. The film is assumed thin so that the ratio of the characteristic lengths $\epsilon = H/L \ll 1$, allowing the application of lubrication theory. This assumption is simply that of a small Marangoni number $\sqrt{\text{Ma}} = \epsilon \ll 1$ and has been used in previous work [10].

The liquid velocities, v'_x and v'_z , and pressure p' are governed by the Navier-Stokes equations with no slip and no penetration at the substrate and stress balances at the liquid-air interface. The film height h' deforms in response to flow in the film and is governed by the kinematic condition. A normal stress balance at the interface reveals that an appropriate scale for the pressure is $p^* = \sigma_0 \epsilon^2 / H$, and an x -momentum balance coupled with the kinematic condition gives the x -velocity scale $v_x^* = \epsilon^3 \sigma_0 / \mu$ and time scale $t^* = H / v_x^* \epsilon$. Finally, bulk mass conservation gives the z -velocity scale $v_z^* = \epsilon v_x^*$ (see the Appendix for a derivation of these scales). Thus, we introduce the dimensionless variables (indicated without a prime superscript):

$$\begin{aligned} x' &= \epsilon^{-1} H x, & z' &= H z, & h' &= H h, & \sigma' &= \sigma_0 \sigma, & c' &= c_0 c, \\ v'_x &= v_x^* v_x, & v'_z &= \epsilon v_x^* v_z, & p' &= p^* p, & t' &= t^* t. \end{aligned} \quad (2)$$

The surface tension σ is assumed to vary linearly with the solute concentration c at the interface according to

$$\sigma = 1 - \text{Ma } c|_{z=h}. \quad (3)$$

This assumes a dilute solute ($\omega_0 \ll 1$) and has been used in many previous studies (e.g., Refs. [10,15,35]). Retaining only leading-order terms in the Navier-Stokes equations yields the lubrication equations governing the liquid velocity and pressure:

$$\frac{\partial^2 v_x}{\partial z^2} = \frac{\partial p}{\partial x}, \quad (4)$$

$$\frac{\partial p}{\partial z} = 0, \quad (5)$$

$$\frac{\partial v_x}{\partial x} + \frac{\partial v_z}{\partial z} = 0. \quad (6)$$

In dimensionless form, the no-slip, no-penetration, normal stress balance, and tangential stress balance give the boundary conditions

$$v_x|_{z=0} = v_z|_{z=0} = 0, \quad (7)$$

$$p|_{z=h} = -\frac{\partial^2 h}{\partial x^2}, \quad (8)$$

$$\left. \frac{\partial v_x}{\partial z} \right|_{z=h} = -\frac{\partial c|_{z=h}}{\partial x}. \quad (9)$$

Note that due to the choice of the lateral domain size $L = H/\sqrt{\text{Ma}}$, the Marangoni number Ma does not appear in tangential stress balance (9). Solving equations (4)–(6) subject to these conditions gives explicit expressions for the liquid velocities:

$$v_x = -\left(\frac{1}{2}z^2 - hz\right) \frac{\partial^3 h}{\partial x^3} - \frac{\partial c|_{z=h}}{\partial x} z, \quad (10)$$

$$v_z = \left(\frac{1}{6}z^3 - \frac{1}{2}hz^2\right) \frac{\partial^4 h}{\partial x^4} + \frac{1}{2} \left(\frac{\partial^2 c|_{z=h}}{\partial x^2} - \frac{\partial h}{\partial x} \frac{\partial^3 h}{\partial x^3}\right) z^2. \quad (11)$$

Mass conservation at the interface $z = h$ requires the kinematic condition

$$v_z = \frac{\partial h}{\partial t} + v_x \frac{\partial h}{\partial x}, \quad (12)$$

and inserting velocities (10) and (11) yields the thin-film equation

$$\frac{\partial h}{\partial t} = \underbrace{-\frac{1}{3} \frac{\partial}{\partial x} \left[h^3 \frac{\partial^3 h}{\partial x^3} \right]}_{\text{capillary flow}} + \underbrace{\frac{1}{2} \frac{\partial}{\partial x} \left[h^2 \frac{\partial c|_{z=h}}{\partial x} \right]}_{\text{Marangoni flow}}. \quad (13)$$

This equation describes the change in film height h over time in terms of contributions from capillary flow and Marangoni flow. It is coupled to the evolution of solute concentration c through Marangoni flow and subject to the initial condition $h_0 = 1$.

B. Solute concentration and initial condition

The solute is assumed to have constant diffusivity D in the solvent and is governed by the dimensionless convection-diffusion equation

$$\frac{\partial c}{\partial t} + v_x \frac{\partial c}{\partial x} + v_z \frac{\partial c}{\partial z} = \frac{1}{\text{Pe}} \frac{\partial^2 c}{\partial x^2} + \frac{1}{\epsilon^2 \text{Pe}} \frac{\partial^2 c}{\partial z^2}. \quad (14)$$

Here, the Péclet number $Pe = H v_x^* / D \epsilon$ gives the ratio between the lateral diffusive and convective time scales. Similarly, $\epsilon^2 Pe$ gives the ratio between the vertical diffusive and convective time scales. Note that Eq. (14) assumes Fickian diffusion in the liquid film.

Previous studies often used one of two approximations to simplify Eq. (14). If the vertical diffusion time is small ($\epsilon^2 Pe \ll 1$), one may solve for a leading-order, vertically uniform concentration profile [15, 17, 32]. However, vertical gradients are large in the system we seek to investigate, so this approximation is not applicable. Studies that include vertical gradients argue that lateral diffusion is negligible, since $\epsilon^2 Pe \ll Pe$, and neglect its contribution in Eq. (14) (e.g., Refs. [4, 10]). We do not neglect lateral diffusion in this work; as will be seen in Secs. III and IV, lateral diffusion plays a key role in the behavior we observe. Therefore, we retain all terms in Eq. (14) and apply no-flux conditions:

$$\left. \frac{\partial c}{\partial z} \right|_{z=0} = 0, \quad \left. \frac{\partial c}{\partial z} \right|_{z=h} - \epsilon^2 \frac{\partial h}{\partial x} \left. \frac{\partial c}{\partial x} \right|_{z=h} = 0. \quad (15)$$

In the experiments of Horiuchi *et al.* [25], a solid substrate was coated with two-layer films consisting of an ethanol-rich bottom layer and an ethanol-depleted top layer. To approximate this two-layer structure, the initial concentration profile has a solute-rich bottom layer and a solute-depleted top layer, achieved by the transition function

$$T(z; h_b, s) = \begin{cases} 1, & w \leq 0 \\ \frac{\exp(-\frac{1}{1-w})}{\exp(-\frac{1}{1-w}) + \exp(-\frac{1}{w})}, & 0 < w < 1 \\ 0, & 1 \leq w, \end{cases} \quad \text{where } w = \frac{z - (h_b - 1/s)}{2/s}. \quad (16)$$

Here, h_b is the dimensionless bottom-layer thickness and s is the slope of the transition between layers. There are numerous other functions that could be used, such as an inverse or hyperbolic tangent function or the Heaviside step function (obtained when $s \rightarrow \infty$). However, the inverse and hyperbolic tangent functions do not satisfy boundary conditions (15) analytically because their derivatives never vanish. Furthermore, a step function is numerically undesirable because it leads to the Gibbs phenomenon when numerical solutions are attempted. In contrast, transition function (16) analytically satisfies no-flux boundary conditions while preserving the spectral accuracy of the numerical method presented in Sec. II C.

The initial condition c_0 is constructed to model a two-layer film with a lateral perturbation to the concentration profile that is initially localized to the diffuse region between layers:

$$c_0(x, z; h_b, s, c_p, \alpha, \nu) = T(z; h_b, s) \left(1 + c_p \cos(\alpha x) e^{-\frac{(z-h_b)^2}{2\nu^2}} \right). \quad (17)$$

Plots of c_0 that are used in Secs. III and IV are shown in Fig. 3. The parameters c_p and α are, respectively, the magnitude and wavenumber of the lateral perturbation while ν is the standard deviation of the Gaussian that localizes the perturbation to the diffuse region between layers. This work takes $s = 3$ and $\nu = 0.1$, and the influence of h_b , c_p , and α is investigated in Sec. IV. The parameter s is fixed at the largest value that is numerically practical, while ν is fixed at a value that strongly localizes the perturbation to the diffuse region. This localization is important when analyzing the effects of h_b as will be shown in Sec. IV C. For the parameters used in this work, the perturbation described in Eq. (17) cannot be seen in Fig. 3 due to its small amplitude but leads to a wealth of interesting behavior.

Actual coating processes are subject to small, effectively random perturbations that arise from vibrations, imperfect mixing, and other sources. The initial condition (17) is a model perturbation that allows us to probe fundamental mechanisms, whereas random noise would involve a distribution of Fourier modes. Thus, for the results presented in Sec. III, accompanying simulations were run where the sinusoidal perturbation in Eq. (17) was replaced with a finite sum of Fourier modes over a uniformly distributed set of wavenumbers and amplitudes to approximate random noise. Only small quantitative shifts were observed in the results using random noise, so those results are not shown.

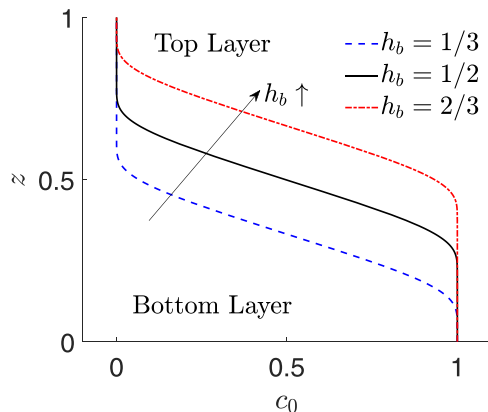


FIG. 3. Cross sections of the initial condition $c_0(x, z)$ for three bottom layer thicknesses h_b at $x = \pi/\alpha$. The top layer corresponds to layer 1 and the bottom layer to layer 2 in Fig. 1. As the bottom layer thickness h_b increases, the transition between layers occurs at larger z (layer 2 is thicker and layer 1 thinner in Fig. 1). The perturbation centered at $z = h_b$ cannot be seen due to its small amplitude.

C. Parameter values and numerical methods

There are two dimensionless groups that appear in convection-diffusion equation (14). The first is the Péclet number Pe , which gives the ratio of the lateral diffusive and convective time scales. The second is the Marangoni number $Ma = \epsilon^2$, which gives the ratio of Marangoni forces to capillary forces but also defines the lateral length scale $L = H/\sqrt{Ma}$. The Marangoni number appears in the lumped parameter $\epsilon^2 Pe = MaPe$ that gives the ratio of the vertical diffusive and convective time scales. Typical values of dimensional and dimensionless parameters are given in Tables I and II, respectively. The effects of varying Pe and Ma are investigated in Secs. III and IV D, respectively.

As formulated in Sec. II B, convection-diffusion equation (14) is subject to the no-flux boundary condition (15) at the moving boundary $z = h(t, x)$. To circumvent numerically solving a moving-boundary problem, the coordinate transformation $(x, z, t) \mapsto (\zeta, \eta, \tau)$ is performed through the relations [4]

$$\eta = \frac{z}{h}, \quad \frac{\partial \zeta}{\partial x} = 1, \quad \frac{\partial \tau}{\partial t} = 1. \quad (18)$$

Here, η is a scaled vertical coordinate, ζ is the lateral coordinate, and τ is the time coordinate. In this new coordinate system, the boundary at $\eta = 1$ is constant in time and space. However, the governing equations become appreciably more complex with the corresponding derivative transformations

$$\frac{\partial}{\partial x} = \frac{\partial}{\partial \zeta} - \frac{\eta}{h} \frac{\partial h}{\partial \zeta} \frac{\partial}{\partial \eta}, \quad \frac{\partial}{\partial z} = \frac{1}{h} \frac{\partial}{\partial \eta}, \quad \frac{\partial}{\partial t} = \frac{\partial}{\partial \tau} - \frac{\eta}{h} \frac{\partial h}{\partial \tau} \frac{\partial}{\partial \eta}. \quad (19)$$

TABLE I. Important dimensional parameters and typical values. Note that, typically, $\Delta\sigma \sim \sigma_0$ [25].

Parameter	Definition	Typical values
H (m)	film thickness	10^{-5} – 10^{-4}
μ (Pa s)	solvent viscosity	10^{-4} – 10^{-3}
σ_0 (N/m)	solvent surface tension	10^{-2} – 10^{-1}
$\Delta\sigma$ (N/m)	solvent/solute surface-tension difference	10^{-2} – 10^{-1}
D (m ² /s)	solute diffusivity	10^{-9}
ω_0	solute mass/mole fraction	10^{-2} – 10^{-1}

TABLE II. Important dimensionless parameters and typical values.

Parameter	Definition	Physical meaning	Typical values
ϵ	$H/L, \sqrt{\text{Ma}}$	vertical length/lateral length	10^{-2} – 10^{-1}
Ma	$\Delta\sigma\omega_0/\sigma_0$	Marangoni forces/surface-tension forces	10^{-3} – 10^{-1}
Pe	$H\sigma_0\epsilon^2/D\mu$	diffusion time/convection time	1 – 10^6

After applying transformation (18) to Eqs. (13) and (14), a pseudospectral method is employed to solve the resulting set of coupled fourth-order nonlinear partial differential equations on the constant domain $\zeta \in (0, 2\pi/\alpha)$ and $\eta \in (0, 1)$ [4,36,37]. Periodic conditions in ζ warrant an expansion in Fourier modes, while the finite domain in η warrants an expansion in Chebyshev polynomials. Therefore, the film height h is expanded in a basis of Fourier modes and the solute concentration c in a tensor-product basis of Fourier modes and Chebyshev polynomials with 20 Fourier modes and 140 Chebyshev polynomials. Furthermore, because the clustering of Chebyshev nodes is poor at resolving features in the center of the domain, the grid is stretched by applying an inverse sine transformation [36,38,39]. Finally, time integration is performed via MATLAB's built-in solver ode15i which is a variable-step, variable-order solver utilizing backward differentiation. The model and numerical method have been verified by reproducing results for pure film leveling and simple cases of one-layer binary films [8,10].

III. NONUNIFORMITIES IN MISCIBLE TWO-LAYER FILMS

We wish to study the mechanisms that may initiate dewetting, so we first discuss the mechanisms through which film-height nonuniformities are generated. With a solute-depleted top layer given by initial condition (17), there is initially no solute present at the interface $z = h$ (see Fig. 3). The lateral concentration defect localized to $z = h_b$ [Eq. (17)] lowers the concentration at $x = \pi/\alpha$ (the lateral center of the film). Thus, there is a smaller vertical concentration gradient driving diffusion toward the interface $z = h$ where $c = 0$. Vertical diffusion is therefore slower near the lateral center of the film, resulting in laterally nonuniform vertical diffusion of solute toward the interface.

Over time, a nonuniform concentration profile that mirrors the imposed defect will develop at the interface. This defect is a depletion of solute in the center of the film, causing a locally high surface tension and Marangoni stresses that drive flow toward the center of the film. As liquid accumulates, a crest in the film height will grow as depicted in Fig. 2. The crest represents a negative curvature of the interface and generates a positive capillary pressure that drives flow to level the crest. In this manner, Marangoni and capillary stresses compete as film-height nonuniformities grow.

Constrained by conservation of mass, the magnitude of concentration gradients and Marangoni stresses is limited and will be matched by capillary stresses if the film does not dewet. Once capillary stresses balance Marangoni stresses, growth of the crest stops and the film reaches its maximally deformed state. Subsequently, lateral diffusion relaxes concentration gradients to return the film to a uniform state. Film height evolution for $\text{Pe} = 10^4$ is shown in Fig. 4(a), where the maximally deformed state (black line) has $\Delta h \approx 4 \times 10^{-2}$ (4% of the film thickness). As evolution continues, the film slowly returns to a uniform state as shown by the profile at $t = 10^4$ (red dashed line). To illustrate the concentration gradients that drive film-height deformation, a maximally deformed state at a larger Péclet number $\text{Pe} = 1.67 \times 10^5$ is given in Fig. 4(b) with the solute concentration contour. Because diffusion is relatively slow, there are significant concentration gradients in both the lateral and vertical directions. As will be discussed in Sec. III B, the vertical gradients can actually contribute to the steepening of the lateral gradients shown in Fig. 4(b). This is the primary driving force for the height perturbation $\Delta h \approx 2 \times 10^{-1}$ (20% of the film thickness) which is nearly an order of magnitude larger than that obtained for $\text{Pe} = 10^4$ in Fig. 4(a).

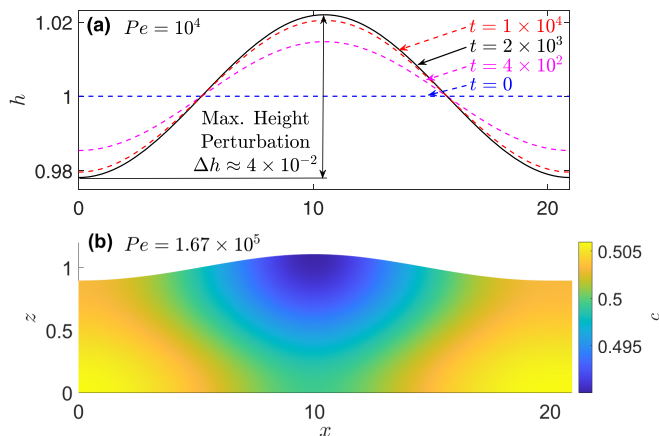


FIG. 4. (a) Time evolution of the film height for $Pe = 10^4$. The maximum height perturbation Δh occurs at $t_{\max} \approx 2 \times 10^3$ where the film-height profile is given by the solid black line. The perturbation slowly decays beyond this time as shown by the profile at $t = 10^4$. (b) Maximally deformed state for $Pe = 1.67 \times 10^5$ with solute concentration contour. This state occurs at $t \approx 9 \times 10^2$ after which the perturbation slowly decays through lateral diffusion. The remaining parameter values are $c_p = 10^{-2}$, $\alpha = 0.3$, $\epsilon = 0.1$, and $h_b = 0.5$.

Figure 4 shows that the value of Pe has a pronounced effect on film evolution. Parameters that play a role include the Péclet number Pe , the Marangoni number Ma , and the bottom-layer thickness h_b . The effects of varying these parameters are investigated in this section (Sec. III), Sec. IV D, and Sec. IV C, respectively. Two important parameters that appear in initial condition (17) are the perturbation magnitude c_p and wavenumber α , investigated in Secs. IV A and IV B. To characterize film nonuniformity and stability as these parameters vary, one may look to the maximum size of the height perturbation Δh and the time required to achieve it t_{\max} . Larger Δh and smaller t_{\max} represent larger nonuniformities that develop more rapidly and thus indicate a less stable film.

For $\epsilon = 0.1$, $\alpha = 0.3$, $c_p = 10^{-2}$, and $h_b = 0.5$, Fig. 5 shows Δh and t_{\max} over a wide range of Pe (red circles) where the labels I, II, and III indicate three distinct parameter regimes. Figure 5(a) shows that Δh increases monotonically through all regions, while Fig. 5(b) shows that t_{\max} has a sharp drop at a critical Péclet number $Pe_{\text{crit}} \approx 10^5$ that indicates the transition into region III. The trends in Fig. 5 result from both the horizontal (Pe) and vertical ($\epsilon^2 Pe$) diffusive time scales

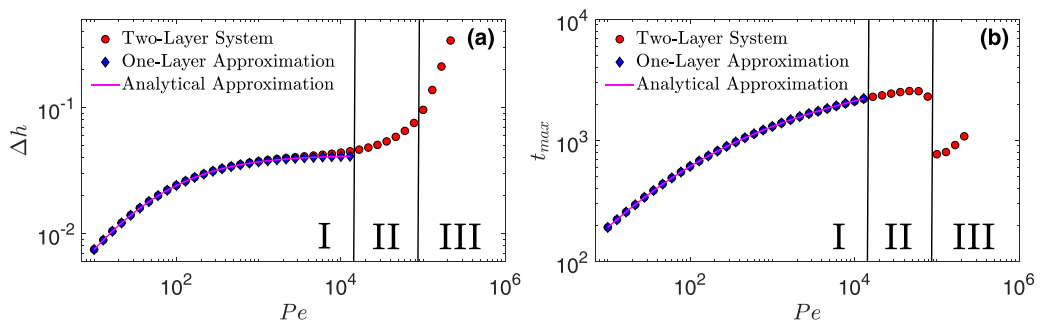


FIG. 5. Plots of (a) the maximum height perturbation Δh and (b) the time to achieve it, t_{\max} , at varying Pe . The plots are divided into three regions labeled I, II, and III. The blue diamond data points are predicted values from the one-layer approximation discussed in Sec. III A, and the solid magenta line is an analytical approximation for region I derived in Sec. III A.

increasing as Pe increases and are discussed by region in Sec. III A (rapid vertical diffusion), Sec. III B (transition region), and Sec. III C (convective steepening).

A. Region I: Rapid vertical diffusion

In region I of Fig. 5, both the maximum height perturbation Δh and the time to achieve it, t_{\max} , increase monotonically. In comparison to regions II and III, region I is at relatively low Pe so diffusion is relatively rapid. If rapid enough, vertical diffusion will quickly smooth out any vertical concentration gradients and the system will behave as if it is vertically uniform. Therefore, we introduce a one-layer approximation where any initial vertical gradients are averaged out of initial condition (17) (this is what rapid vertical diffusion would achieve):

$$\overline{c_0}(x) = \int_0^1 c_0(x, z) dz = \underbrace{\int_0^1 T(z; h_b, s) dz}_{\text{base state } c_b} + c_p \underbrace{\int_0^1 T(z; h_b, s) e^{-\frac{(z-h_b)^2}{2v^2}} dz}_{\text{perturbation magnitude } \overline{c_p}} \cos(\alpha x). \quad (20)$$

Equation (20) has contributions from a uniform base state c_b and a lateral sinusoidal perturbation with magnitude $\overline{c_p}$. Governing equations (13) and (14) are numerically solved from the initial condition $\overline{c_0}$ (rather than c_0) to yield the one-layer approximation shown in region I of Fig. 5 (blue diamonds). There is excellent agreement with the two-layer system, indicating that, in region I, vertical diffusion is sufficiently rapid to smooth out vertical gradients before the film begins to deform appreciably. This corresponds to the condition $\epsilon^2 Pe \ll t_{\max}$, which is valid throughout region I as shown by the values of t_{\max} in Fig. 5(b) (recall that $\epsilon = 0.1$).

Having established that vertical diffusion is rapid in region I of Fig. 5, we address the trends in Δh and t_{\max} . Increasing Pe corresponds to increasing the lateral diffusion time scale. Consequently, lateral concentration gradients decay less over a given time, resulting in larger Marangoni stresses and thus larger film-height perturbations. This mechanism can be described by a simple scaling relation, derived by considering thin-film equation (13) when growth of the crest has stopped ($\partial h/\partial t = 0$). At this time, capillary stresses balance Marangoni stresses and thin-film equation (13) reduces to

$$h \frac{\partial^3 h}{\partial x^3} = \frac{3}{2} \frac{\partial c|_{z=h}}{\partial x}. \quad (21)$$

With rapid diffusion, the concentration perturbation magnitude is well approximated by decay of the initial magnitude $\overline{c_p}$ through diffusion by the factor $\exp(-\alpha^2 t_{\max}/Pe)$. This factor can be obtained by considering purely lateral diffusion. Noting that $h \sim 1$ and $\partial/\partial x \sim \alpha$ (due to periodicity), we have the relation

$$\Delta h \sim \alpha^{-2} \overline{c_p} \exp(-\alpha^2 t_{\max}/Pe). \quad (22)$$

Relation (22) predicts an increase in Δh with increasing Pe due to slowing diffusion, and shows a scaling with α^{-2} that arises from the ratio of capillary stresses $\sim \alpha^4$ and Marangoni stresses $\sim \alpha^2$ in height-evolution equation (13). Furthermore, relation (22) reveals that the height perturbation Δh scales linearly with the concentration perturbation magnitude $\overline{c_p}$. Therefore, with $\overline{c_p} \ll 1$, a perturbation expansion in powers of $\overline{c_p}$ for both the film height h and solute concentration c may yield useful insight. We expand both unknowns as

$$h = 1 + \overline{c_p} h_1(t, x) + O(\overline{c_p}^2), \quad c = c_b + \overline{c_p} c_1(t, x) + O(\overline{c_p}^2), \quad (23)$$

where c_b is the base state indicated in Eq. (20). Because vertical diffusion is rapid, we have assumed that c is uniform in z for simplicity. However, one could instead employ the rapid-vertical-diffusion approximation proposed by Jensen and Grothberg [17] without affecting the results of this analysis.

Substituting Eqs. (23) into Eqs. (13) and (14) gives the $O(\overline{c_p})$ problem

$$\frac{\partial h_1}{\partial t} = -\frac{1}{3} \frac{\partial^4 h_1}{\partial x^4} + \frac{1}{2} \frac{\partial^2 c_1}{\partial x^2}, \quad \frac{\partial c_1}{\partial t} = \frac{1}{Pe} \frac{\partial^2 c_1}{\partial x^2} \quad (24)$$

with initial conditions $h_1 = 0$ and $c_1 = \cos(\alpha x)$. The latter of Eqs. (24) has the solution

$$c_1 = \cos(\alpha x) \exp\left(-\frac{\alpha^2}{\text{Pe}}t\right), \quad (25)$$

which shows that c_1 is simply the initial perturbation decaying over time due to lateral diffusion. Substituting this form for c_1 into the former of Eqs. (24) gives the fourth-order, linear, inhomogeneous partial differential equation governing h_1 :

$$\frac{\partial h_1}{\partial t} = -\frac{1}{3} \frac{\partial^4 h_1}{\partial x^4} - \frac{\alpha^2}{2} \cos(\alpha x) \exp\left(-\frac{\alpha^2}{\text{Pe}}t\right). \quad (26)$$

Given the nonconstant forcing term in Eq. (26), as well as the eigenfunctions of the fourth-derivative operator, it is sensible to expect the x dependence of h_1 to be a cosine wave. Thus, we assume $h_1 = \cos(\alpha x)g(t)$ with $g(0) = 0$, and Eq. (26) has the solution

$$h_1(t, x) = \frac{\alpha^2/2}{\alpha^4/3 - \alpha^2/\text{Pe}} \cos(\alpha x) \left(\exp\left(-\frac{\alpha^4}{3}t\right) - \exp\left(-\frac{\alpha^2}{\text{Pe}}t\right) \right). \quad (27)$$

The constant coefficient in solution (27) is proportional to the magnitude of Marangoni stresses $\alpha^2/2$ and inversely related to those of capillary flow $\alpha^4/3$ and lateral diffusion α^2/Pe . This agrees with intuition, since stronger Marangoni stresses (larger $\alpha^2/2$) result in larger $g(t)$ and thus larger height perturbations. Similarly, considering also the transient part of Eq. (27) suggests that stronger capillary stresses or faster diffusion results in smaller height perturbations. Summarizing, the expressions for the height h and concentration c to $O(\bar{c}_p^{-2})$ are

$$c = c_b + \bar{c}_p \cos(\alpha x) \exp\left(-\frac{\alpha^2}{\text{Pe}}t\right) + O(\bar{c}_p^{-2}), \quad (28)$$

$$h = 1 + \bar{c}_p \frac{\alpha^2/2}{\alpha^4/3 - \alpha^2/\text{Pe}} \cos(\alpha x) \left(\exp\left(-\frac{\alpha^4}{3}t\right) - \exp\left(-\frac{\alpha^2}{\text{Pe}}t\right) \right) + O(\bar{c}_p^{-2}), \quad (29)$$

which describe the film dynamics in region I of Fig. 5. From these solutions, we can obtain explicit expressions for Δh and t_{\max} ; the amplitude of h gives the size of the height perturbation over time and exhibits a unique maximum at time

$$t_{\max} = \frac{\log(\alpha^4/3) - \log(\alpha^2/\text{Pe})}{\alpha^4/3 - \alpha^2/\text{Pe}} + O(\bar{c}_p). \quad (30)$$

Equation (30) is the inverse of the logarithmic-mean difference of the magnitudes of capillary stresses $\alpha^4/3$ and lateral diffusion α^2/Pe , where an increase in either results in a decrease in t_{\max} . Intuitively, stronger capillary stresses more quickly counteract Marangoni stresses, and stronger lateral diffusion more quickly levels lateral concentration gradients. However, the logarithmic-mean difference also suggests a form of nonlinear physical ‘‘exchange’’ (notably arising in heat exchangers) [40]. Indeed, faster lateral diffusion leads to smaller capillary stresses because it more quickly levels concentration gradients. This causes smaller Marangoni stresses and thus smaller height perturbations which create smaller capillary stresses. In contrast, larger capillary stresses more quickly counteract Marangoni stresses and allow less time for lateral diffusion, reducing its importance. Therefore, an increase in either capillary stresses ($\alpha^4/3$) or lateral diffusion (α^2/Pe) reduces the importance of the other. This exchange through the medium of Marangoni stresses is encapsulated in Eq. (30). Capillary stresses, Marangoni stresses, and solute diffusion are interdependent in this manner.

Concluding this analysis, we substitute Eq. (30) for t_{\max} into Eq. (29) for h and solve for the amplitude to obtain an explicit expression for the maximum height perturbation Δh :

$$\Delta h = 3\bar{c}_p \alpha^{-2} \exp\left(-\frac{\alpha^2}{\text{Pe}}t_{\max}\right) + O(\bar{c}_p^{-2}). \quad (31)$$

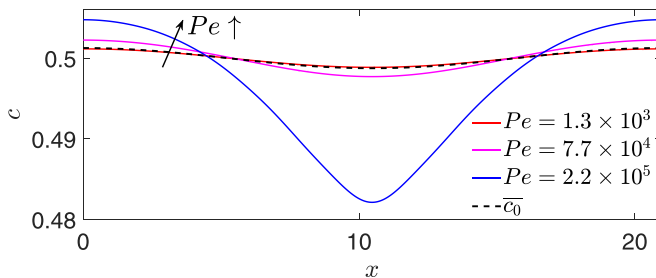


FIG. 6. Concentration profiles at the interface $z = h$ and $t = t_{\max}$ for three different Pe and the vertically averaged initial condition \bar{c}_0 [Eq. (20)]. Under pure diffusion, \bar{c}_0 gives the maximum possible lateral perturbation at the interface. The red line for $Pe = 1.3 \times 10^3$ depicts data taken from region I of Fig. 5. Similarly, the magenta line for $Pe = 7.7 \times 10^4$ and the blue line for $Pe = 2.2 \times 10^5$ are data taken from regions II and III, respectively, of Fig. 5.

This matches scaling relation (22) derived by considering the magnitude of capillary and Marangoni stresses. Equations (30) and (31) are plotted in region I of Fig. 5 (magenta line) where there is excellent agreement between the two-layer system (red circles), one-layer approximation (blue diamonds), and analytical approximation (magenta line). Therefore, the two-layer system quantitatively behaves as a one-layer film at low Pe (in region I) due to rapid vertical diffusion with dynamics well described by Eqs. (28) and (29). Discussion of the dependence on c_p and α is left to Secs. IV A and IV B.

We have established simple mechanisms and analytical expressions for the trends in both Δh and t_{\max} in region I of Fig. 5. Through a one-layer approximation, we established that the two-layer system quantitatively behaves as a one-layer film. Consequently, the maximum film-height perturbation Δh increases with Pe according to Eq. (31) because lateral diffusion slows. Similarly, Eq. (30) shows that t_{\max} increases with Pe according to the inverse of the logarithmic-mean difference of the magnitudes of capillary flow $\alpha^4/3$ and lateral diffusion α^2/Pe .

B. Region II: Transition region

The boundary between region I and region II of Fig. 5 is taken to be the smallest Pe for which Δh for the two-layer system deviates from the one-layer approximation value by more than 10%. Notably, the one-layer approximation plateaus at $\Delta h \approx 3\bar{c}_p\alpha^{-2}$ [as $Pe \rightarrow \infty$ in Eq. (31)] while Δh for the two-layer system continues to increase. While the 10% criterion is arbitrary, it provides a consistent and quantitative distinction between regions I and II. In region II, both the maximum height perturbation Δh and the time to achieve it, t_{\max} , increase monotonically until a critical Péclet number $Pe_{\text{crit}} \approx 10^5$ where t_{\max} drops precipitously and the system is considered to be in region III. We will see that region II contains the transition from the diffusion-dominated, low- Pe region I to the convection-dominated, high- Pe region III.

As Pe increases and the system enters region II of Fig. 5, deviation from the one-layer approximation suggests that the rapid-vertical-diffusion assumption is failing; vertical diffusion becomes sufficiently slow that vertical solute concentration gradients begin to influence film evolution. The increase in Δh in region II shows that Marangoni stresses become larger over a relatively small range of Pe (compared to region I). Furthermore, a precipitous drop in t_{\max} at $Pe_{\text{crit}} \approx 10^5$ indicates a significant shift in the evolution dynamics. To uncover the role of vertical gradients in these phenomena, we examine the solute concentration profiles that drive film-height deformation. Figure 6 shows concentration profiles evaluated at the interface $z = h$ at $t = t_{\max}$ for three different Pe as well as the vertically averaged initial condition \bar{c}_0 defined by Eq. (20). Examining these profiles, we see that the concentration perturbation at the interface drastically increases in magnitude as Pe increases.

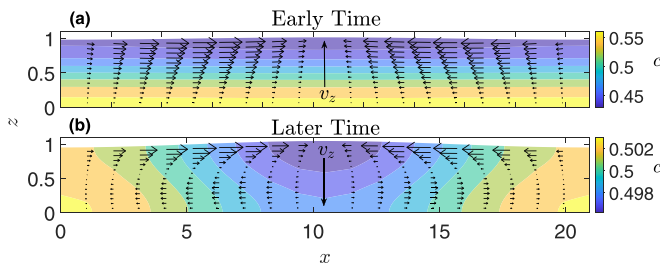


FIG. 7. Velocity contours (black arrows) plotted over solute concentration contours (a) before ($t \approx 2.23 \times 10^2$) and (b) after ($t \approx 6.85 \times 10^2$) the development of circulatory flow for $Pe = 10^5$. The vertical velocity v_z is generally an order of magnitude smaller than the horizontal velocity v_x and is difficult to discern. As a visual aid, the arrows labeled “ v_z ” indicate the direction of the vertical velocity at the center of the film ($x = \pi/\alpha$) but are not to scale. At early times, there is bulk flow from the troughs to the crest. Later, circulatory flow develops while the troughs and crest continue to grow.

As discussed in Sec. III A, vertical diffusion is laterally nonuniform and causes lateral concentration gradients to develop at the interface. Starting from initial condition c_0 [Eq. (17)], vertical diffusion brings the system to a vertically uniform state that coincides with its vertical average, \bar{c}_0 [Eq. (20)]. Thus, \bar{c}_0 gives the largest lateral gradient that will develop at the interface solely from nonuniform vertical diffusion and is plotted in Fig. 6 (dashed black line). The lateral perturbation in \bar{c}_0 gives a limiting value for Marangoni stresses in the one-layer approximation used for region I of Fig. 5, resulting in the plateau $\Delta h \approx 3\bar{c}_p\alpha^{-2}$ [as $Pe \rightarrow \infty$ in Eq. (31)]. Indeed, for $Pe = 1.3 \times 10^3$ (red line), which is in region I, Fig. 6 shows that the concentration profile has not exceeded this limit. However, for $Pe = 7.7 \times 10^4$ (magenta line), which is in region II, Fig. 6 shows that the concentration perturbation exceeds the diffusion-dominated profile \bar{c}_0 . Furthermore, for $Pe = 2.2 \times 10^5$ (blue line), which is in region III, Fig. 6 shows that the concentration profile significantly deviates from the diffusion-dominated profile \bar{c}_0 with a notably deep trough. The sharpening of concentration gradients for larger Pe shows that we have departed from the one-layer approximation and thus diffusion cannot be the mechanism that is sharpening gradients. Therefore, it must be that convection is sharpening gradients since it is the only other process through which solute is transported in the film.

To understand the role of solute convection, we examine the liquid velocity profiles. Figure 7 shows velocity profiles (black arrows) plotted over solute concentration contours at two different times. At early times [Fig. 7(a)], Marangoni stresses drive flow from the troughs (edges) to the crest (center), resulting in a lateral velocity v_x that is positive on the left ($x < \pi/\alpha$) and negative on the right ($x > \pi/\alpha$). The corresponding vertical velocity v_z is positive in the center ($|x - \pi/\alpha| < \pi/2\alpha$) and negative on the edges. Note that the velocities do not change sign through the film depth. At later times, the film has deformed appreciably ($\approx 10\%$ of the film thickness) and capillary stresses become significant. Figure 7(b) shows that the velocity profiles become circulatory with v_x now changing sign about halfway through the film depth. However, the vertical velocity does not change sign through the film depth, and is now negative in the center and positive on the edges. These velocity profiles are reminiscent of cellular structures observed in previous work [10–13], and while a few of these works studied thermal Marangoni flow, analogous phenomena are seen in solutal Marangoni flow. However, we observe unique phenomena due to large vertical concentration gradients from the two-layer geometry.

Due to large vertical concentration gradients, vertical convection can move a significant quantity of solute to or from the interface $z = h$. Keeping in mind that vertical concentration gradients are negative ($\partial c/\partial z < 0$), Fig. 7(a) shows that, at early times, vertical convection increases the solute concentration at the crest (center where $v_z > 0$) and decreases it at the troughs (edges where $v_z < 0$). This effectively counteracts the imposed perturbation which is a depletion of solute in

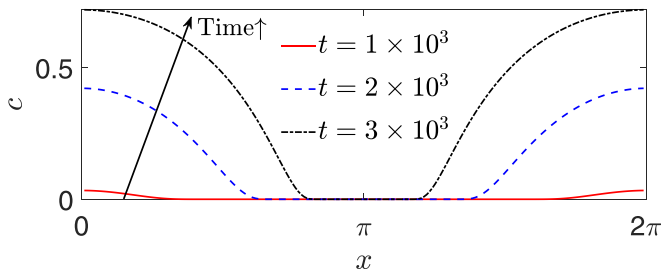


FIG. 8. Solution (35) of convection equation (32) evaluated at $z = 1$ and three different times. Laterally nonuniform vertical convection causes the rapid formation of a laterally nonuniform concentration profile, even though the initial condition is laterally uniform with $c_0^*(z = 1) = 0$.

the center [Eq. (17)]. However, at later times shown in Fig. 7(b), vertical convection acts to increase concentration at the troughs (where $v_z > 0$) and decrease it at the crest (where $v_z < 0$). This steepens the imposed concentration perturbation, causing larger Marangoni stresses and thus larger height perturbations. Convective steepening of lateral concentration gradients causes the sharpening of the concentration profiles shown in Fig. 6 and thus the deviation from the one-layer approximation in Fig. 5 as Pe increases. Large vertical concentration gradients are critical to this phenomenon, since the regions of high concentration near $z = 0$ in Fig. 7 are convected up to the interface $z = h$ by the vertical velocity v_z .

The steepening of lateral concentration gradients from vertical convection is not unique to this system; it can be observed in an analytical solution for solute undergoing pure convection from a laterally uniform initial condition:

$$\frac{\partial c}{\partial t} + u_x(x, z) \frac{\partial c}{\partial x} + u_z(x, z) \frac{\partial c}{\partial z} = 0, \quad c_0^*(z) = T(z; h_b = 1/2, s = 3). \quad (32)$$

The laterally uniform initial condition c_0^* is analogous to c_0 given by Eq. (17), except that it lacks a lateral perturbation. The velocities, u_x and u_z , are chosen to approximate those shown in Fig. 7(b) with

$$u_x(x, z) = u_m z \sin(x), \quad u_z(x, z) = \frac{u_m}{2} z^2 \cos(x). \quad (33)$$

Here, u_x does not change sign through the film depth, which misses the recirculation shown in Fig. 7, and approximation (33) does not conserve mass. However, the important phenomenon is vertical convection and the approximation u_z is qualitatively correct with $u_z < 0$ near the center ($x = \pi$) and $u_z > 0$ near the edges. The parameter u_m controls the maximum value of the velocity, which we take as $u_m = 9 \times 10^{-4}$ to approximate values observed in the numerical model.

On the constant domain $x \in (0, \pi)$ and $z \in (0, \infty)$, we solve Eq. (32) by the method of characteristics to obtain

$$z(t) = z_0 \sqrt{\frac{\sin(x(t))}{\sin(x_0)}}, \quad x(t) = f^{-1}\left(f(x_0) + u_m \frac{z_0}{\sqrt{\sin(x_0)}} t\right). \quad (34)$$

The function f , along with a full derivation of these characteristics, is provided in the Appendix. These characteristics are numerically inverted to obtain values for $z_0(t, x, z)$ with which the solution to Eq. (32) is

$$c(t, x, z) = c_0^*(z_0(t, x, z)). \quad (35)$$

Solution (35) is plotted for $z = 1$ as a function of x and three different times in Fig. 8. Although the initial profile c_0^* [Eq. (32)] is laterally uniform, the x dependence of the vertical velocity u_z [Eq. (33)] couples with vertical concentration gradients to create lateral concentration gradients.

The velocities shown in Fig. 7(b) that are approximated by Eqs. (33) require that the interface has deformed appreciably so that capillary stresses are significant. Recalling that there is initially no solute at the interface (see Fig. 3), some degree of vertical diffusion must have already occurred to develop lateral concentration gradients and Marangoni stresses that deform the interface. As Pe increases and vertical diffusion slows, larger vertical concentration gradients are present in the system at any given time, and particularly when the liquid velocities become circulatory as shown in Fig. 7(b). Thus, vertical convection will more rapidly steepen lateral concentration gradients resulting in the increasing Δh we observe in region II of Fig. 5(a). One can observe how rapid convective steepening is in the analytical example plotted in Fig. 8, where concentration gradients that are orders of magnitude larger than those shown in Fig. 6 have developed on time scales similar to values observed for t_{\max} in Fig. 5(b). Once Pe is large enough that the lateral gradients rapidly created by convective steepening significantly exceed those from nonuniform vertical diffusion, we observe the precipitous drop in t_{\max} at $Pe_{\text{crit}} \approx 10^5$. Beyond this drop, convective steepening is the dominant mechanism causing film-height deformation. Thus, region II represents the transition from the diffusion-dominated region I to the convection-dominated region III.

C. Region III: Convective steepening

In region III of Fig. 5, convective steepening of lateral concentration gradients is the primary mechanism for film-height deformation as discussed in Sec. III B. Throughout region III of Fig. 5, the vertical diffusion time scale $\epsilon^2 Pe$ is comparable to, or greater than, the deformation time t_{\max} , so significant vertical gradients are present for all times $t \leq t_{\max}$. Therefore, convective steepening creates increasingly large and sharp lateral concentration gradients as shown by the profile at $Pe = 2.2 \times 10^5$ in Fig. 6 (blue line). The increase in the height perturbation Δh in region III of Fig. 5 accelerates as Pe increases because of these increasingly sharp concentration gradients.

After the initial precipitous drop at $Pe_{\text{crit}} \approx 10^5$ in Fig. 5, t_{\max} begins to increase. This is partially due to increasing vertical diffusion times, that scale as $\epsilon^2 Pe$, since there is an initial diffusion time required to develop a lateral gradient at the interface. However, this is not the scaling we observe in region III of Fig. 5(b) (a linear fit gives a power-law exponent ≈ 0.74) because there is an additional contribution from capillary stresses. As was discussed in Sec. III A and demonstrated in Eq. (30), larger height perturbations create larger capillary stresses that inhibit growth and increase t_{\max} . Coupled with longer vertical diffusion times, this gives the increase in t_{\max} we see in Fig. 5(b). Note that Eq. (30) was derived for region I and thus does not predict t_{\max} in regions II or III. However, the physical mechanisms of capillary flow and diffusion that it embodies are present in all regions.

With an understanding of all three regions of Fig. 5, it is worthwhile to discuss their relation to an actual coating process. Films are solidified for many applications, so there is a solidification time t_{solid} that may be from evaporation, curing, or other methods. (Note that solidification is not considered in this work and could introduce additional phenomena, e.g., film deformation due to development of stresses in the solid.) In the solidified film, it is likely desirable that the two layers remain uniform and distinct to impart different functionality to each layer [25,41]. Thus, solidification should be more rapid than vertical diffusion and the formation of nonuniformities ($t_{\text{solid}} \ll \epsilon^2 Pe$ and $t_{\text{solid}} \ll t_{\max}$). Figure 9 shows schematics of possible solidified film geometries for values of Pe in the three regions of Fig. 5. Despite small height perturbations, it is unlikely that region I is favorable because any distinction between layers is quickly erased by diffusion, resulting in one uniform layer as shown in Fig. 9(a); the restriction $t_{\text{solid}} \ll \epsilon^2 Pe$ requires extremely rapid solidification that could introduce additional instabilities [10]. Thus, region II or region III is more desirable because slower diffusion allows one to achieve stratified layers as depicted in Figs. 9(b) and 9(c). However, film-height nonuniformities are significantly larger in region III than those in regions I and II due to convective steepening. Furthermore, t_{\max} drops precipitously at Pe_{crit} as shown in Fig. 5(b), so the restriction $t_{\text{solid}} \ll t_{\max}$ is more difficult to achieve in region III. Therefore, region II may be the optimal region for a two-layer coating process, since height perturbations are

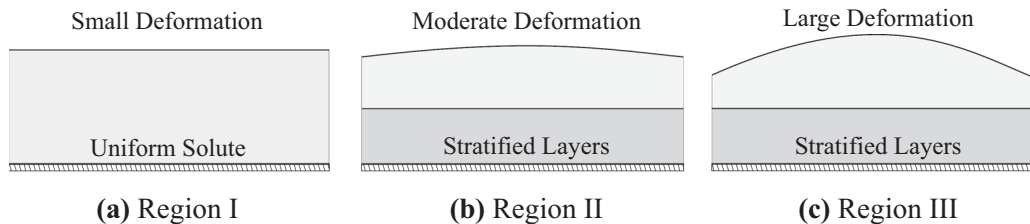


FIG. 9. Schematics depicting possible geometries of a solidified film for values of the Péclet number Pe in (a) region I, (b) region II, and (c) region III of Fig. 5.

small relative to region III [see Fig. 5(a)] and Pe and t_{\max} are large enough that the restrictions $t_{\text{solid}} \ll \epsilon^2 Pe$ and $t_{\text{solid}} \ll t_{\max}$ are not too strict.

IV. EFFECTS OF SYSTEM PARAMETERS

In this section we conduct a parametric study to understand the influence of system parameters on film evolution. In a two-layer coating, there are a number of physical parameters that affect film dynamics. Physical properties of the liquid are encapsulated in the two dimensionless groups Pe and Ma . The dependence on the Péclet number Pe was explored in Sec. III, and the dependence on the Marangoni number Ma will be investigated in Sec. IV D. The system geometry is controlled by the dimensionless bottom-layer thickness h_b and is explored in Sec. IV C. The two parameters that control the perturbation imposed in initial condition (17) are the magnitude c_p and wavenumber α , investigated in Secs. IV A and IV B, respectively. The remaining parameters, $s = 3$ and $\nu = 0.1$, are fixed as discussed in Sec. II B.

A. Perturbation magnitude

The perturbation magnitude c_p controls the magnitude of the imposed lateral perturbation in initial condition (17). While difficult to control in a coating process, it is important to understand how the size of perturbations affects film stability. In Sec. III, the perturbation magnitude was taken to be $c_p = 10^{-2}$ which is 1% of the base-state concentration. While numerical limitations (due to steep concentration gradients) prevent us from generating meaningful data at larger c_p , we can uncover the basic trends by examining film evolution at smaller c_p . Results for $c_p = 10^{-2}$ are given again in Figs. 10(a) and 10(b) along with results using two smaller values, $c_p = 10^{-3}$ and $c_p = 10^{-4}$. Figure 10(a) shows that the magnitude of the height perturbation Δh increases monotonically as c_p increases. In contrast, Fig. 10 shows that, remarkably, the t_{\max} for all three values of c_p are visually indistinguishable, suggesting that the size of the initial concentration perturbation does not appreciably affect the time scales for film evolution.

To understand this behavior, we return to Eqs. (30) and (31). In region I (rapid vertical diffusion; see Sec. III A), Eq. (31) reveals that the maximum height perturbation Δh scales linearly with the initial concentration perturbation c_p , while Eq. (30) shows that t_{\max} is independent of c_p . Linear fits of Δh at each Pe show a linear scaling with c_p for all Pe investigated in this work. Selected values of Pe are shown in Fig. 10(c), where the largest value is taken in region III. Remarkably, we see the linear scaling with c_p that was derived for region I holds through regions II and III, suggesting that the lateral concentration gradients that result from convective steepening (see Sec. III B) scale linearly with c_p . Furthermore, Fig. 10(b) shows that t_{\max} is independent of c_p for all regions, even though Eq. (30) only holds in region I. We note that we were unable to obtain analytical relations for regions II and III due to the complexity of convective steepening of concentration gradients. Nevertheless, Fig. 10 shows that while the maximum deformation achieved, Δh , scales linearly with the perturbation magnitude c_p , so does the rate at which the film deforms, resulting in a deformation time t_{\max} that is effectively independent of c_p for all Pe investigated in this work.

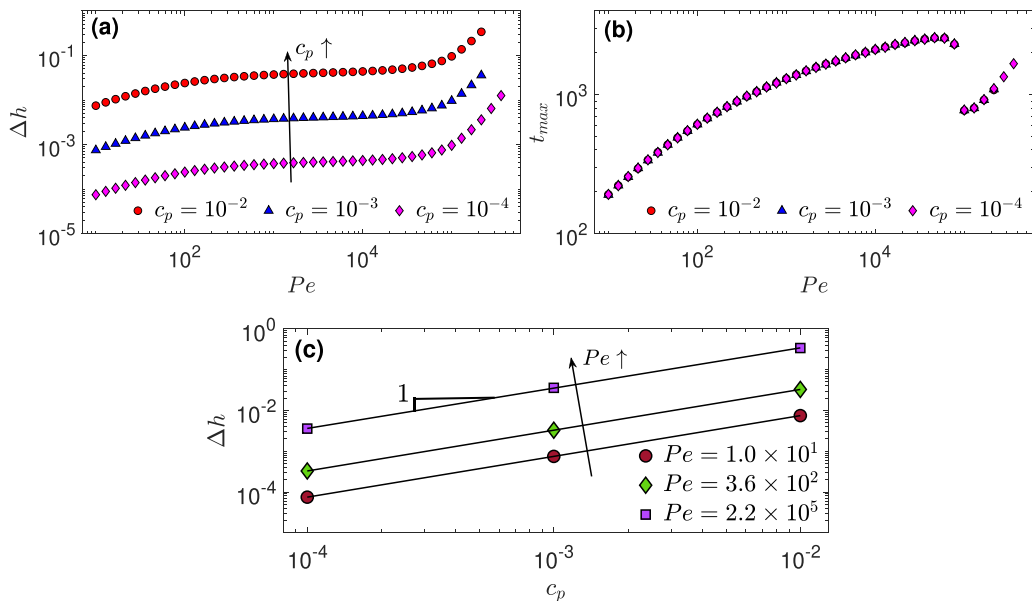


FIG. 10. (a) The maximum height perturbation Δh and (b) the time to achieve it, t_{\max} , at varying Pe and three perturbation magnitudes c_p . There are only quantitative shifts in Δh , and the values of t_{\max} are nearly identical for all three values of c_p . (c) Linear fits of the maximum height perturbation Δh versus perturbation magnitude c_p at three different Pe . All lines have a slope of approximately unity, indicating a linear scaling with c_p . The largest value of $Pe = 2.2 \times 10^5$ is taken from region III where an analytical scaling relation has not been derived.

This analysis has revealed that the perturbation magnitude c_p has a direct effect on film stability. If a coating process tends to introduce larger perturbations into a coated film, the resulting film-height nonuniformities will be larger, scaling linearly with the perturbation magnitude c_p . Furthermore, even though the maximum film-height nonuniformities are larger, the times to achieve them are unchanged; this is a surprising result that can be understood from the analysis in Sec. III A. Larger height perturbations bring the film to a more nonuniform state, and thus larger c_p is destabilizing. One should strive to minimize the magnitude of lateral concentration perturbations in two-layer coatings for optimal uniformity.

B. Perturbation wavenumber

The perturbation wavenumber α controls the period of the imposed lateral perturbation in initial condition (17). Due to periodicity, the dimensionless lateral domain is $x \in (0, 2\pi/\alpha)$, and thus α controls the dimensionless lateral length scale $2\pi/\alpha$. There are numerous lateral derivatives that appear in Eqs. (13) and (14), so the effect of varying α is difficult to predict *a priori*. As shown in Figs. 11(a) and 11(b), varying α has a pronounced effect on both the maximum height perturbation Δh and the time to achieve it, t_{\max} .

In region I (rapid vertical diffusion; see Sec. III A), the decrease in Δh and t_{\max} with increasing α is quantitatively predicted by Eqs. (30) and (31). Equation (31) may be rewritten in the form

$$\log \alpha^2 \Delta h \sim -\frac{\alpha^2 t_{\max}}{Pe}. \quad (36)$$

Linear fits of the data from Figs. 11(a) and 11(b) for three different Pe are shown in Fig. 11(c) where we see that Eq. (36) captures the trends in Δh and t_{\max} as α varies in region I (red circles and green diamonds) but not in regions II and III (purple squares) where convective steepening becomes

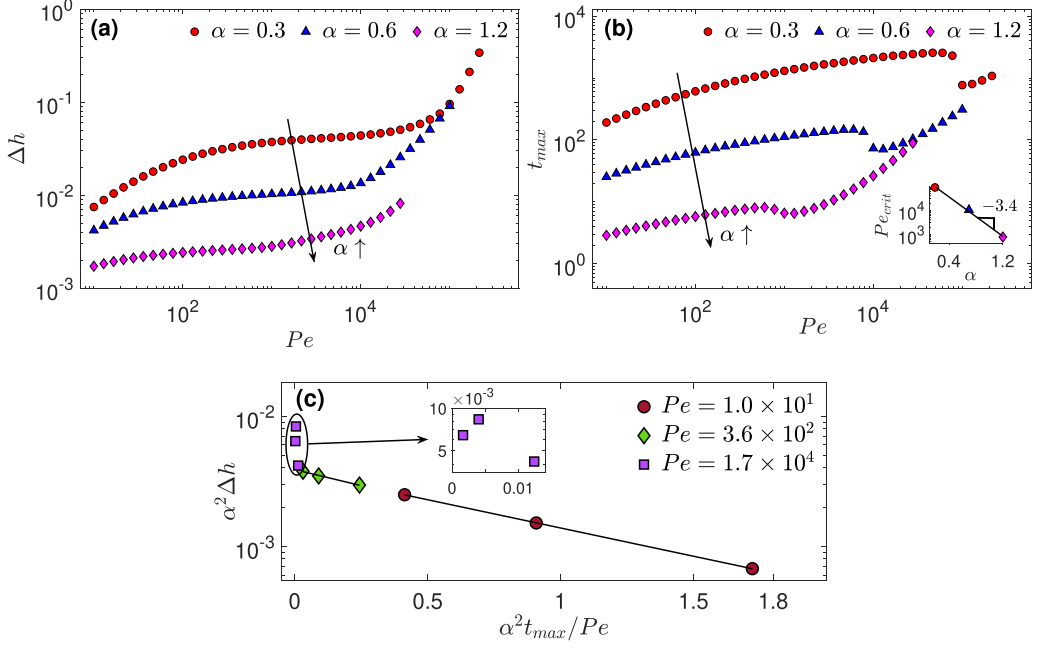


FIG. 11. (a) The maximum height perturbation Δh and (b) the time to achieve it, t_{max} , at different Pe and three perturbation wavenumbers α . (c) Linear fits of the scaled height perturbation $\alpha^2 \Delta h$ versus the scaled time $\alpha^2 t_{max} / Pe$. Data points for $Pe = 1.7 \times 10^4$ in regions II and III are repeated in the zoomed-in subplot to illustrate that the scaling relation does not hold outside of region I.

important. As α is increased in region I, lateral diffusion more quickly levels the higher-wavenumber concentration gradients resulting in reduced Marangoni stresses. Furthermore, higher wavenumber disturbances result in a larger interfacial curvature and thus stronger capillary stresses which more quickly counteract Marangoni stresses. Together, these effects result in the decrease of Δh and t_{max} in region I of Figs. 10(a) and 10(b) that is described by Eqs. (30) and (31). The evolution is more complicated in regions II and III, however, where we see nonmonotonic trends arising in both Δh and t_{max} at large Pe . To understand this, we first investigate the dependence of Pe_{crit} on α and then establish a qualitative understanding of the trends in regions II and III.

In Fig. 11(b), we observe that Pe_{crit} (at which t_{max} drops) decreases as α increases. As discussed in Sec. III B, the drop in t_{max} at Pe_{crit} occurs when vertical diffusion is sufficiently slow that convective steepening is the dominant mechanism creating lateral concentration gradients at the interface. Considering the center of the film where $v_x = 0$ ($x = \pi/\alpha$ in Fig. 7), we can isolate relevant terms in Eq. (14):

$$v_z \frac{\partial c}{\partial z} \sim \frac{1}{\epsilon^2 Pe_{crit}} \frac{\partial^2 c}{\partial z^2}. \quad (37)$$

To extract a useful relation from Eq. (37), we assume that vertical derivatives are independent of α because α does not affect the vertical length scale. We then rewrite Eq. (11) as

$$v_z = \underbrace{\frac{1}{6}(\eta^3 - 3\eta^2) \frac{\partial}{\partial \zeta} \left[h^3 \frac{\partial^3 h}{\partial \zeta^3} \right]}_{\text{capillary flow}} + \underbrace{\frac{1}{2} \eta^2 \frac{\partial}{\partial \zeta} \left[h^2 \frac{\partial c}{\partial \zeta} \Big|_{z=1} \right]}_{\text{Marangoni flow}} + \eta \frac{\partial h}{\partial \zeta} v_x. \quad (38)$$

Recalling that $v_x = 0$ in the center of the film, v_z [Eq. (38)] has clear contributions from capillary flow and Marangoni flow. The contribution from capillary flow is negative due to the crest in the

film height, while the contribution from Marangoni flow is positive because the solute concentration is minimum in the center of the film. Figure 7(b) shows that $v_z < 0$ in the center of the film at later times, so capillary flow must be dominant. Furthermore, the capillary-flow term scales as α^4 , and thus $v_z \sim \alpha^4$. Inserting this into relation (37) reveals

$$\text{Pe}_{\text{crit}} \sim \epsilon^{-2} \alpha^{-4}. \quad (39)$$

This approximates the relation shown in a subplot in Fig. 11(b), where linear regression reveals the scaling $\text{Pe}_{\text{crit}} \sim \alpha^{-3.4}$. The discrepancy in the power-law exponent of relation (39) is likely due to the assumption that the vertical derivatives are independent of α ; the relation $v_z \sim \alpha^4$ requires that the qualitative shift in the velocities shown in Fig. 7 has occurred, which in turn requires that some time has passed. This time is tied to the growth of the height disturbance, which must become sufficiently large so that capillary flow overcomes Marangoni flow in Eq. (38). Over this time, which is dependent on α , vertical gradients will relax through diffusion. Thus, the size of vertical gradients depends on α in a way that is difficult to capture through scaling relations. However, the data in Fig. 11(b) show that this dependence is somewhat weak, resulting in the small discrepancy in the exponents of the predicted scaling $\text{Pe}_{\text{crit}} \sim \alpha^{-4}$ and observed scaling $\text{Pe}_{\text{crit}} \sim \alpha^{-3.4}$ for the range of α investigated here.

Now, we examine the trends in region II (transition between regions I and III; see Sec. III B) and region III (after the drop in t_{max} ; see Sec. III C) of Figs. 11(a) and 11(b). The increase in Δh with Pe is monotonic, with Δh steeply increasing at lower Pe as α is increased. This is due to an earlier transition into region III described by relation (39); in this region, convection is stronger and thus more rapidly steepens concentration gradients. These steepened gradients result in larger Marangoni stresses and thus larger Δh . This is especially pronounced at $\text{Pe} = 10^5$, where Δh for $\alpha = 0.6$ (blue triangle) has begun to exceed that for $\alpha = 0.3$ (red circle). Thus, the trend in Δh with α is not necessarily monotonic at large Pe due to the complexity of convective steepening.

The accompanying trend in t_{max} can be understood with similar reasoning, where faster diffusion and stronger capillary stresses at larger α reduce t_{max} according to Eq. (30). The quantity t_{max} more rapidly increases at larger α due to capillary stresses in Eq. (13) which scale as $\alpha^4 \Delta h$. Because the size of the height perturbation Δh rapidly increases with Pe [as shown in Fig. 11(a)], the damping of growth rates ($\partial h / \partial t$) by capillary stresses also rapidly increases with Pe. Furthermore, this damping scales as α^4 , and is thus even more pronounced at larger α . These effects become so prominent that the trend in t_{max} with α is not necessarily monotonic at large Pe, with t_{max} in Fig. 11(b) at $\text{Pe} = 2.8 \times 10^4$ being nearly equal for $\alpha = 0.6$ (blue triangle) and $\alpha = 1.2$ (magenta diamond).

This analysis has shown that the effect of α on film stability is complex. In region I where Pe is small, we see that an increase in α decreases both Δh and t_{max} according to Eqs. (30) and (31). While a decrease in Δh is stabilizing, a decrease in t_{max} is destabilizing. Furthermore, the situation is more complicated at large Pe where we find that the trend in both Δh and t_{max} is not monotonic with α . The role of perturbation wavelengths in film stability is thus strongly dependent on the value of the Péclet number Pe. In a physical coating process, small, effectively random perturbations result in a distribution of wavenumbers where the width of the coated film controls smallest wavenumber α that can be expressed in the perturbation. A smaller coated width will generally result in larger wavenumbers giving larger height deformations Δh as well as larger deformation times t_{max} . However, at very large Pe, these relationships may reverse, with an increase in α giving a decrease in Δh or t_{max} depending on the value of Pe. One must thus be cognizant of the value of the Péclet number when considering the effects of film width and perturbation wavenumbers on film stability.

C. Layer thickness

Initial condition (17) approximates the conditions studied by Horiuchi *et al.* [25] as a binary miscible two-layer film with a diffuse boundary between layers. The parameter h_b gives an effective bottom-layer thickness and is an important parameter in two-layer coating that influences many

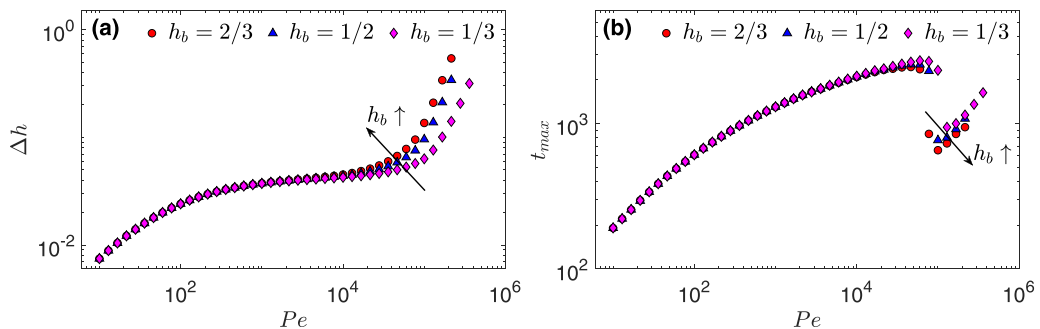


FIG. 12. Plots of (a) the maximum height perturbation Δh and (b) the time to achieve it, t_{\max} , at different Pe and three layer thicknesses h_b . There are only small quantitative shifts in both Δh and t_{\max} .

aspects of the coating process [25,42]. Here we focus on how h_b influences the maximum height perturbation Δh and the time to achieve it, t_{\max} . Values of Δh and t_{\max} at three different bottom-layer thicknesses h_b are given in Fig. 12. Notably, both Δh and t_{\max} at different h_b are indistinguishable in region I, but begin to diverge from each other slightly in region II and noticeably in region III (see Sec. III for a discussion of each region).

The lack of dependence on h_b in region I is due to the form of initial condition (17), where the perturbation is localized to the diffuse region between layers. Marangoni flow is the result of concentration gradients, so it is not affected by the base state value c_b in Eq. (20). Furthermore, the Gaussian in the perturbation magnitude \bar{c}_p integrand decays sufficiently fast that the integrand is near zero outside of the diffuse region. The diffuse region has radius $1/s$, so with $\nu = 0.1$ and $s = 3$ we have $1/s \approx 3\nu$; approximately 99.8% of the Gaussian distribution lies within three standard deviations of the mean, so the perturbation magnitude integrand in Eq. (20) decays to essentially zero outside of the diffuse region. It is thus expected that h_b has no appreciable effect on region I of Fig. 12 because it has a negligible effect on the perturbation magnitude. While this may seem to be an artifact of the form chosen for c_0 , it is actually a decoupling of the parameters h_b and c_p that aids this parametric study.

As Pe increases into regions II and III, the convective steepening mechanism described in Sec. III B becomes important and a dependence on h_b emerges. Steepening of lateral concentration gradients requires vertical concentration gradients that can be nonuniformly convected to the interface $z = h$. The largest vertical gradients are precisely at $z = h_b$, so decreasing h_b moves the largest vertical gradients farther from the interface and closer to the substrate where vertical convection is weaker due to the no-penetration condition. Thus, convective steepening is weaker and steepens lateral concentration gradients less. This is reflected in Fig. 12, where we see Δh for $h_b = 1/3$ (magenta diamonds) falls below $h_b = 1/2$ (blue triangles), which in turn falls below $h_b = 2/3$ (red circles). However, t_{\max} shows the opposite ordering in region III, because a smaller bottom layer necessitates more time for vertical concentration gradients to be nonuniformly convected up to the interface.

It is clear that decreasing the bottom-layer thickness h_b has a stabilizing effect on the film. While changing h_b has little effect in region I, there is a noticeable effect in region III. When h_b is reduced, the maximum height perturbation Δh decreases and the time to achieve it, t_{\max} , increases. Both of these effects are stabilizing, so reducing the bottom-layer thickness h_b has a small but stabilizing effect. This stabilizing effect is primarily due to vertical concentration gradients being positioned farther from the interface and closer to the substrate where convection is weaker. If the perturbation in initial condition (17) was not localized to the diffuse region between layers, decreasing h_b would also reduce the averaged perturbation magnitude \bar{c}_p [Eq. (20)] because it reduces the amount of perturbed liquid. One may return to the analyses in Secs. III A and IV A to see that decreasing the perturbation magnitude results in smaller Δh .

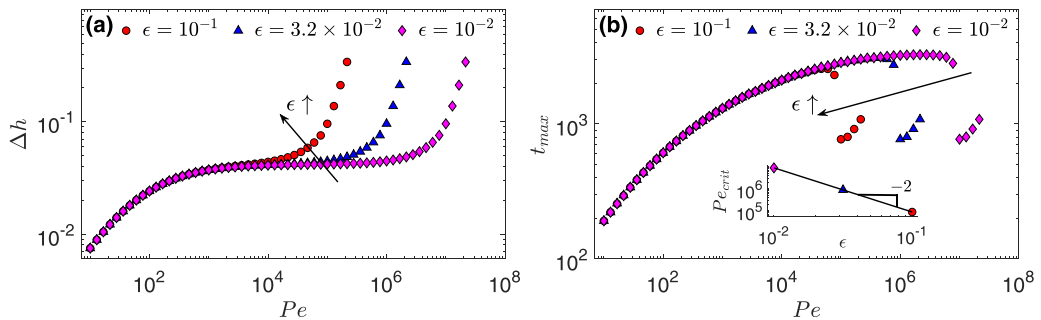


FIG. 13. Plots of (a) the maximum height perturbation Δh and (b) the time to achieve it, t_{\max} , at varying Péclet number Pe and three different Marangoni numbers $Ma = \epsilon^2$. There are only quantitative shifts in where region transitions occur. The inset plot in (b) shows the scaling $Pe_{\text{crit}} \sim \epsilon^{-2}$.

While there are a number of differences between the model developed in this work and the experiments of Horiuchi *et al.* [25], we can make some qualitative comparisons. Horiuchi *et al.* [25] found that decreasing the bottom-layer thickness of their films inhibited dewetting. In this work, we have found a similar trend, where decreasing h_b improves film stability by reducing the film-height perturbation Δh and increasing the time to achieve it, t_{\max} . Our work thus suggests that the improved stability observed by Horiuchi *et al.* [25] may be caused by vertical concentration gradients being positioned farther from the liquid-air interface.

D. Marangoni number

The Marangoni number $Ma = \epsilon^2$ gives the ratio of Marangoni forces to capillary forces. While this quantity is crucial to the scaling of physical variables used in Eqs. (2) and defines the lateral length scale $L = H/\sqrt{Ma}$, it only appears once in the final governing equations as the lumped parameter $\epsilon^2 Pe$ in Eq. (14). This controls the vertical diffusion time scale, and thus reducing Ma has the sole effect of reducing the vertical diffusion time. Figure 13 shows results for Δh and t_{\max} for three different $\epsilon = \sqrt{Ma}$ and varying Pe . We see that at $\epsilon = 10^{-2}$ the film remains in regions I and II until $Pe_{\text{crit}} \approx 10^7$, whereas for $\epsilon = 10^{-1}$ the transition occurs at $Pe_{\text{crit}} \approx 10^5$. Recalling scaling relation (39) that predicts $Pe_{\text{crit}} \sim \epsilon^{-2}$, this is precisely the trend we see in Fig. 13(b) where an inset plot shows a linear fit of Pe_{crit} to ϵ . Because reducing Ma simply reduces the vertical diffusion time scale, a larger Pe is required for vertical diffusion to be sufficiently slow for the convective steepening mechanism discussed in Sec. III B to become important.

Caution should be taken in interpreting these results from a stability standpoint. Increasing Ma has the direct effect of decreasing Pe_{crit} , which may be considered destabilizing since convective steepening becomes significant at lower Pe . In addition, the parameter $\epsilon = \sqrt{Ma}$ appears numerous times in physical scales (2), and namely in the time scale $t^* = H/v_x^* \epsilon \sim \epsilon^{-4}$. Therefore, decreasing ϵ increases the physical time scale, so while the dimensionless times presented in Fig. 13 may be similar, the corresponding dimensional times are not. Namely, t_{\max} for smaller Ma are actually larger and thus, coupled with the shift in Pe_{crit} , decreasing Ma is stabilizing. This is perhaps unsurprising, since smaller Ma indicates weaker Marangoni forces which should be stabilizing. Therefore, multilayer coatings comprised of liquids with similar surface tensions will exhibit smaller film-height nonuniformities than those comprised of liquids with significantly different surface tensions.

We again compare our results to those reported by Horiuchi *et al.* [25], where it was found that decreasing the Marangoni number Ma inhibited dewetting. We have found a similar trend, where decreasing $\epsilon = \sqrt{Ma}$ improves film stability by shifting Pe_{crit} to higher values. Thus, our model suggests that the improved stability observed by Horiuchi *et al.* [25] may be due to a transition into

a more stable region (e.g., region III to region II) with smaller film-height perturbations Δh as Pe_{crit} increases.

V. CONCLUSIONS

In this work, we characterized the evolution of film-height nonuniformities in nonvolatile miscible two-layer binary films. From momentum and mass conservation, we derived a set of evolution equations that predict the time evolution of film height and solute concentration. These equations assume the liquid has constant viscosity and density, that the solute is sufficiently dilute ($\omega_0 \ll 1$), and that the Marangoni number is sufficiently small. Because the liquid layers are miscible, there is no liquid-liquid interface and the two-layer system is captured through an initial condition for the concentration that changes value sharply between layers.

Rather than attempting a quantitative comparison with the motivating experiments of Horiuchi *et al.* [25], we developed fundamental understanding of the mechanisms that generate film-height nonuniformities in two-layer miscible films. Capturing the effects of large vertical concentration gradients absent in previous work, we found that a disparity in initial solute concentration between the film layers drives flows that lead to significant film-height nonuniformities. Subsequently, through a parametric study, we examined how system parameters influence this behavior and developed scaling relations that shed light on the physical mechanisms underlying the observations of Horiuchi *et al.* [25].

It was found that three distinct parameter regimes arise when the Péclet number Pe is varied. In region I where Pe is small, vertical diffusion is rapid and the evolution of the two-layer film is quantitatively that of a one-layer film. Using this fact, analytical relations were derived that predict the evolution of film-height nonuniformities in region I. In region II at moderate Pe , diffusion time scales are sufficiently large that circulatory velocities, reminiscent of those observed in previous work [10–13], cause a rapid steepening of lateral concentration gradients. This phenomenon is unique to the two-layer system, as it is not observed in region I (one-layer films). Finally, in region III at large Pe , convective steepening only becomes more pronounced as diffusion slows and leads to significant film-height nonuniformities. It was determined that region II is likely the optimal region for a two-layer coating process, since height perturbations are small and develop slowly and vertical diffusion is slow enough that solidification need not be too rapid to retain stratified layers.

With an understanding of the dependence on Pe , a parametric study was conducted for the remaining system parameters. It was found that the magnitude of the initial concentration perturbation c_p has a direct effect on film stability; a larger perturbation results in larger film-height nonuniformities and thus a less stable film. The effect of the perturbation wavenumber α is complex since intricate dependencies between capillary and Marangoni stresses lead to trends that are strongly dependent on the value of Pe . It was then found that decreasing the bottom-layer thickness h_b has a stabilizing effect because it hinders convective steepening of the concentration profiles. Finally, it was found that the Marangoni number $Ma = \epsilon^2$ directly controls the critical Péclet number Pe_{crit} at which the system transitions into region III. Furthermore, decreasing Ma has a stabilizing effect on the film, increasing Pe_{crit} and the times required to develop film-height nonuniformities. Predictions of the model appear to be in qualitative agreement with the experiments of Horiuchi *et al.* [25].

There are several promising extensions of this work. First, it is possible that the solute and solvent have widely separated viscosities [25]. Concentration gradients will then lead to significant viscosity gradients, the effects of which are difficult to predict and warrant a numerical investigation [4,14,43]. Second, in deriving the mathematical model, we neglected the influence of evaporation and thermal Marangoni flows. However, evaporation has been shown to have a wide range of effects on film dynamics [10,18,19]. Extending the model to drying films is a necessary extension of this work because industrial coatings often undergo drying. Drying films also often contain polymers or colloidal particles that allow the film to solidify, so including the influence of a polymer solute or colloidal particles is a third promising extension of this work that may introduce a number of complex phenomena [19,20].

ACKNOWLEDGMENTS

This work was supported by the Industrial Partnership for Research in Interfacial and Materials Engineering of the University of Minnesota. We also acknowledge partial support through a fellowship awarded to C.L. by the PPG Foundation.

APPENDIX

1. Derivation of characteristic scales

To obtain the scales used in Eq. (2), we begin by noting that the initial film height H provides a scale for z' and h' . Then, from lubrication theory, the lateral length scale $L = H/\epsilon$ is used for x' , where $\epsilon = H/L \ll 1$. Denoting the scales for the lateral velocity v'_x and the vertical velocity v'_z as v_x^* and v_z^* , respectively, the continuity equation

$$\frac{\partial v'_x}{\partial x'} + \frac{\partial v'_z}{\partial z'} = 0 \quad (\text{A1})$$

implies $v_z^* = \epsilon v_x^*$. From the kinematic condition,

$$v'_z = \frac{\partial h'}{\partial t'} + v'_x \frac{\partial h'}{\partial x'},$$

we obtain the scale t^* for t' as $t^* = H/v_x^* \epsilon$.

Now, substituting these scales into the x -momentum balance

$$\rho \left(\frac{\partial v'_x}{\partial t'} + v'_x \frac{\partial v'_x}{\partial x'} + v'_z \frac{\partial v'_x}{\partial z'} \right) = -\frac{\partial p'}{\partial x'} + \mu \left(\frac{\partial^2 v'_x}{\partial x'^2} + \frac{\partial^2 v'_x}{\partial z'^2} \right)$$

and assuming $\epsilon \text{Re} \ll 1$, where the Reynolds number $\text{Re} = \rho v_x^* H / \mu$, we obtain the pressure scale $p^* = \mu v_x^* / H \epsilon$. The normal-stress balance is, at leading order,

$$p' = -\frac{\partial^2 h'}{\partial x'^2} \sigma'. \quad (\text{A2})$$

Substituting the scales obtained above and using $\sigma' \sim \sigma_0$ gives an expression for the velocity scale $v_x^* = \epsilon^3 \sigma_0 / \mu$.

The result that appears in Eq. (1) is obtained from the tangential-stress balance, which at leading order is

$$\mu \frac{\partial v'_x}{\partial z'} = -\frac{\partial \sigma'}{\partial x'}. \quad (\text{A3})$$

The left-hand side scales as $\mu v_x^* / H$, and the right-hand side scales as $\Delta \sigma \omega_0 / L$. Substituting $v_x^* = \epsilon^3 \sigma_0 / \mu$ gives Eq. (1).

2. Solution of convection equation

In this section we derive characteristics (34) used in Sec. III B of the main text. The method of characteristics seeks characteristic curves $(t, x(t), z(t))$ on which the solution to Eqs. (32) is constant. This leads to the system of nonlinear ordinary differential equations

$$\frac{\partial x}{\partial t} = v_m z \sin(x), \quad \frac{\partial z}{\partial t} = \frac{v_m}{2} z^2 \cos(x), \quad (\text{A4})$$

subject to the initial conditions $x = x_0$ and $z = z_0$. This system is autonomous, allowing us to seek a solution for z of the form $z = z(x(t))$ so that

$$\frac{\partial z}{\partial t} = \frac{\partial z}{\partial x} \frac{\partial x}{\partial t}. \quad (\text{A5})$$

Inserting the time derivatives from Eq. (A4) and simplifying yields

$$\frac{1}{z} \frac{\partial z}{\partial x} = \frac{1}{2} \cot(x) \Rightarrow z(x(t)) = z_0 \sqrt{\frac{\sin(x(t))}{\sin(x_0)}}. \quad (\text{A6})$$

We then substitute this form for $z(x(t))$ into the former of Eqs. (A4) and integrate to obtain the implicit solution for $x(t)$,

$$\int_{x_0}^{x(t)} \frac{1}{\sin^{3/2}(y)} dy = v_m \frac{z_0}{\sqrt{\sin(x_0)}} t. \quad (\text{A7})$$

The integral in this solution is not trivial to evaluate; skipping some intermediate details, the key is to rewrite the integrand and then integrate by parts, giving

$$\int_{x_0}^{x(t)} \frac{1}{\sin^{3/2}(y)} dy = \int_{x_0}^{x(t)} \sqrt{\sin(y)} \csc^2(y) dy = -2 \frac{\cos(y)}{\sqrt{\sin(y)}} \Big|_{x_0}^{x(t)} - \int_{x_0}^{x(t)} \sqrt{\sin(y)} dy. \quad (\text{A8})$$

Through the change of variable $Y = \frac{1}{4}(\pi - 2y)$, the latter integral can be rewritten in terms of E , the elliptic integral of the second kind:

$$\int_{x_0}^{x(t)} \sqrt{\sin(y)} dy = -2 \int_{Y_0}^Y \sqrt{1 - 2 \sin^2(Y)} dY = -2E \left(\frac{1}{4}(\pi - 2y) \mid 2 \right) \Big|_{x_0}^{x(t)}. \quad (\text{A9})$$

Denoting the function f as

$$f(x) = 2E \left(\frac{1}{4}(\pi - 2x) \mid 2 \right) - 2 \frac{\cos(x)}{\sqrt{\sin(x)}} \quad (\text{A10})$$

and putting together Eqs. (A7)–(A9) yields

$$\int_{x_0}^{x(t)} \frac{1}{\sin^{3/2}(y)} dy = f(y) \Big|_{x_0}^{x(t)} \Rightarrow x(t) = f^{-1} \left(f(x_0) + v_m \frac{z_0}{\sqrt{\sin(x_0)}} t \right). \quad (\text{A11})$$

-
- [1] C. K. Buerkin, I. de Vries, S. M. Raupp, P. Scharfer, W. Schabel, and P. Groen, Investigation of interfacial instabilities with a two-layer slide coating process, *J. Coat. Technol. Res.* **14**, 991 (2017).
- [2] P. Koliopoulos, K. S. Jochem, R. K. Lade, L. F. Francis, and S. Kumar, Capillary flow with evaporation in open rectangular microchannels, *Langmuir* **35**, 8131 (2019).
- [3] S. Karki, H. Kim, S. J. Na, D. Shin, K. Jo, and J. Lee, Thin films as an emerging platform for drug delivery, *Asian J. Pharm. Sci.* **11**, 559 (2016).
- [4] M. Dey, A. S. Vivek, H. N. Dixit, A. Richhariya, and J. J. Feng, A model of tear-film breakup with continuous mucin concentration and viscosity profiles, *J. Fluid Mech.* **858**, 352 (2019).
- [5] R. J. Braun, T. A. Driscoll, C. G. Begley, P. E. King-Smith, and J. I. Siddique, On tear film breakup (TBU): Dynamics and imaging, *Math. Med. Biol.* **35**, 145 (2018).
- [6] M. Schmitt, S. Raupp, D. Wagner, P. Scharfer, and W. Schabel, Analytical determination of process windows for bilayer slot die coating, *J. Coat. Technol. Res.* **12**, 877 (2015).
- [7] C. Giroto, B. P. Rand, J. Genoe, and P. Heremans, Exploring spray coating as a deposition technique for the fabrication of solution-processed solar cells, *Sol. Energy Mater. Sol. Cells* **93**, 454 (2009).
- [8] A. Oron, S. H. Davis, and S. G. Bankoff, Long-scale evolution of thin liquid films, *Rev. Mod. Phys.* **69**, 931 (1997).
- [9] R. V. Craster and O. K. Matar, Dynamics and stability of thin liquid films, *Rev. Mod. Phys.* **81**, 1131 (2009).
- [10] S. K. Serpetsi and S. G. Yiantsios, Stability characteristics of solutocapillary Marangoni motion in evaporating thin films, *Phys. Fluids* **24**, 122104 (2012).

- [11] J. R. A. Pearson, On convection cells induced by surface tension, *J. Fluid Mech.* **4**, 489 (1958).
- [12] L. E. Scriven and C. V. Sterlning, On cellular convection driven by surface-tension gradients: Effects of mean surface tension and surface viscosity, *J. Fluid Mech.* **19**, 321 (1964).
- [13] C. V. Sterlning and L. E. Scriven, Interfacial turbulence: Hydrodynamic instability and the Marangoni effect, *AIChE J.* **5**, 514 (1959).
- [14] S. G. Yiantsios, S. K. Serpetsi, F. Doumenc, and B. Guerrier, Surface deformation and film corrugation during drying of polymer solutions induced by Marangoni phenomena, *Int. J. Heat Mass Transf.* **89**, 1083 (2015).
- [15] T. Pham, X. Cheng, and S. Kumar, Drying of multicomponent thin films on substrates with topography, *J. Polym. Sci., Part B: Polym. Phys.* **55**, 1681 (2017).
- [16] M. Rodríguez-Hakim, J. M. Barakat, X. Shi, E. S. G. Shaqfeh, and G. G. Fuller, Evaporation-driven solutocapillary flow of thin liquid films over curved substrates, *Phys. Rev. Fluids* **4**, 034002 (2019).
- [17] O. E. Jensen and J. B. Grotberg, The spreading of heat or soluble surfactant along a thin liquid film, *Phys. Fluids A* **5**, 58 (1993).
- [18] J. P. Burelbach, S. G. Bankoff, and S. H. Davis, Nonlinear stability of evaporating/condensing liquid films, *J. Fluid Mech.* **195**, 463 (1988).
- [19] S. G. Yiantsios and B. G. Higgins, Marangoni flows during drying of colloidal films, *Phys. Fluids* **18**, 082103 (2006).
- [20] A. F. Routh and W. B. Zimmerman, Distribution of particles during solvent evaporation from films, *Chem. Eng. Sci.* **59**, 2961 (2004).
- [21] L. Merklein, M. Mink, D. Kourkoulos, B. Ulber, S. M. Raupp, K. Meerholz, P. Scharfer, and W. Schabel, Multilayer OLEDs with four slot die-coated layers, *J. Coat. Technol. Res.* **16**, 1643 (2019).
- [22] V. Derflinger, Multilayer hard coating for tools, U.S. Patent No. 7,618,720 (2009).
- [23] J. C. Grunlan, Multilayer coating for flame retardant substrates, U.S. Patent No. 9,540,763 (2012).
- [24] R. Belden, Multilayer coating with visual effect, International Patent Application No. 2017/066604 (2017).
- [25] R. Horiuchi, W. J. Suszynski, and M. S. Carvalho, Simultaneous multilayer coating of water-based and alcohol-based solutions, *J. Coat. Technol. Res.* **12**, 819 (2015).
- [26] K. D. Danov, V. N. Paunov, N. Alleborn, H. Raszillier, and F. Durst, Stability of evaporating two-layered liquid film in the presence of surfactant - I. The equations of lubrication approximation, *Chem. Eng. Sci.* **53**, 2809 (1998).
- [27] K. D. Danov, V. N. Paunov, S. D. Stoyanov, N. Alleborn, H. Raszillier, and F. Durst, Stability of evaporating two-layered liquid film in the presence of surfactant - II. Linear analysis, *Chem. Eng. Sci.* **53**, 2823 (1998).
- [28] V. N. Paunov, K. D. Danov, N. Alleborn, H. Raszillier, and F. Durst, Stability of evaporating two-layered liquid film in the presence of surfactant - III. Non-linear stability analysis, *Chem. Eng. Sci.* **53**, 2839 (1998).
- [29] J. Nam and M. S. Carvalho, Linear stability analysis of two-layer rectilinear flow in slot coating, *AIChE J.* **56**, 2503 (2010).
- [30] A. Kalogirou, Instability of two-layer film flows due to the interacting effects of surfactants, inertia, and gravity, *Phys. Fluids* **30**, 030707 (2018).
- [31] S. Ghosh, R. Usha, and K. C. Sahu, Linear stability analysis of miscible two-fluid flow in a channel with velocity slip at the walls, *Phys. Fluids* **26**, 014107 (1994).
- [32] B. Tsai, M. S. Carvalho, and S. Kumar, Leveling of thin films of colloidal suspensions, *J. Colloid Interface Sci.* **343**, 306 (2010).
- [33] R. V. Craster and O. K. Matar, Numerical simulations of fingering instabilities in surfactant-driven thin films, *Phys. Fluids* **18**, 032103 (2006).
- [34] B. D. Edmonstone, O. K. Matar, and R. V. Craster, A note on the coating of an inclined plane in the presence of soluble surfactant, *J. Colloid Interface Sci.* **293**, 222 (2006).
- [35] G. Vazquez, E. Alvarez, and J. M. Navaza, Surface tension of alcohol + water from 20 to 50 °C, *J. Chem. Eng. Data* **40**, 611 (1995).

- [36] J. P. Boyd, *Chebyshev and Fourier Spectral Methods: Second Revised Edition* (Dover Publications, Mineola, NY, 2001).
- [37] L. N. Trefethen, *Spectral methods in MATLAB* (Society for Industrial and Applied Mathematics (SIAM), Philadelphia, PA, 2000).
- [38] D. Kosloff and H. Tal-Ezer, A modified Chebyshev pseudospectral method with an $O(N^{-1})$ time step restriction, *J. Comput. Phys.* **104**, 457 (1993).
- [39] J. L. Mead and R. A. Renaut, Optimal Runge-Kutta methods for first order pseudospectral operators, *J. Comput. Phys.* **152**, 404 (1999).
- [40] M. Mistry and R. Misener, Optimising heat exchanger network synthesis using convexity properties of the logarithmic mean temperature difference, *Comput. Chem. Eng.* **94**, 1 (2016).
- [41] M. Schulz and J. L. Keddie, A critical and quantitative review of the stratification of particles during the drying of colloidal films, *Soft Matter* **14**, 6181 (2018).
- [42] J. Nam and M. S. Carvalho, Mid-gap invasion in two-layer slot coating, *J. Fluid Mech.* **631**, 397 (2009).
- [43] M. Dizechi and E. Marschall, Viscosity of some binary and ternary liquid mixtures, *J. Chem. Eng. Data* **27**, 358 (1982).